First-order Raman scattering of rare-earth containing *i*-MAX single crystals $(Mo_{2/3}RE_{1/3})_2AlC$ (RE = Nd, Gd, Dy, Ho, Er)

A. Champagne,[1] O. Chaix-Pluchery,[2] T. Ouisse,[2] D. Pinek,[2] I. Gélard,[2] L. Jouffret,[3] M. Barbier,[2,4] F. Wilhelm,[4] Q. Tao,[5] J. Lu,[5] J. Rosen,[5] M. W. Barsoum,[6] and J.-C. Charlier[1]

[1]*Institute of Condensed Matter and Nanoscience, UCLouvain, B-1348 Louvain-la-Neuve, Belgium*

[2]*Univ. Grenoble Alpes, CNRS, Grenoble INP, LMGP, F-38000 Grenoble, France*

[3]*Université Clermont Auvergne, CNRS, SIGMA Clermont, Institut de Chimie de Clermont-Ferrand, F-63000 Clermont-Ferrand, France*

[4]*European Synchrotron Radiation Facility, CS40220, F-38043 Grenoble Cedex 9, France*

[5]*Thin Film Physics, Department of Physics, Chemistry and Biology (IFM), Linköping University, SE-58183 Linköping, Sweden*

[6]*Department of Materials Science and Engineering, Drexel University, Philadelphia, Pennsylvania 19104, USA*

(Received 1 April 2019; published 31 May 2019)

Herein, we report on the growth of single crystals of various $(Mo_{2/3}RE_{1/3})_2AlC$ (RE = Nd, Gd, Dy, Ho, Er) *i*-MAX phases and their Raman characterization. Using first principles, the wave numbers of the various phonon modes and their relative atomic displacements are calculated and compared to experimental results. Twelve high-intensity Raman peaks are identified as the fingerprint of this new family of rare-earth containing *i*-MAX phases, thus being a useful tool to investigate their corresponding composition and structural properties. Indeed, while a redshift is observed in the low-wave-number range due to an increase of the rare-earth atomic mass when moving from left to right on the lanthanide row, a blueshift is observed for most of the high-wave-number modes due to a strengthening of the bonds. A complete classification of bond stiffnesses is achieved based on the direct dependence of a phonon mode wave number with respect to the bond stiffness. Finally, STEM images are used to confirm the crystal structure.

DOI: 10.1103/PhysRevMaterials.3.053609

I. INTRODUCTION

The ternary machinable, nanolamellar carbides and nitrides, with formula $M_{n+1}AX_n$ also known as MAX phases, comprise a family of more than 150 layered hexagonal crystal structures (space group $P6_3/mmc$) [1]. They are composed of two-dimensional (2D) $M_{n+1}X_n$ sheets separated by A layers, where M represents an early transition metal, A an element from groups 13 to 16, X either a carbon or a nitrogen atom, and n varies from 1 to 3. By now, it is well established that at least a subset of MAX phases combine some of the best properties of metals and ceramics [1–3]. including high electrical and thermal conductivities, chemical, oxidation, and thermal shock resistances, as well as reversible deformation [4] and bulk ripplocations [5,6].

In 2011, a new family of 2D materials, called MXenes, was discovered, resulting from the selective etching of A layers from the parent MAX phases [7]. Thanks to their versatile chemistry and the control of their surface terminations, MXenes are quickly becoming the largest family of 2D materials competing in an impressive number of applications [8–19]. Recently, a new route to increase the elemental combinations possible by the addition of a fourth element to the parent MAX phase has been discovered [20–22]. Historically, most quaternary MAX phases existed as random solid solutions. In 2014, out-of-plane ordered quaternary MAX phases (*o*-MAX), such as Cr_2TiAlC_2, Mo_2TiAlC_2, and Mo_2ScAlC_2, were discovered [23]. In 2017, in-plane ordered quaternary MAX phases (*i*-MAX) were theoretically predicted and successfully synthesized with the formula $(M^1_{2/3}M^2_{1/3})_2AlC$, where M^1 and M^2 are two metals in-plane ordered [24,25]. The first *i*-MAX phase reported was $(Mo_{2/3}Sc_{1/3})_2AlC$ [24]. Very recently, 11 new *i*-MAX phases with rare-earth (RE) elements with the chemical formula $(M_{2/3}RE_{1/3})_2AlC$ were discovered [26]. Almost simultaneously, a similar layered family with a $M_4RE_4Al_7C_3$ stoichiometry was discovered [27]. Since all these new MAX phases are Al-based, their conversion to 2D MXenes using chemical exfoliation should, in principle, be possible.

Single crystal growth has been previously reported for several MAX phases [28–30], including Ti_3SiC_2, Cr_2AlC, and V_2AlC. Large single crystals have been used to study their magnetotransport [31,32], electronic [33], and vibrational properties [34]. In addition, utilizing single crystal palette as precursor for synthesizing large area 2D MXene is also promising. In this context, a first step consists in the growth and characterization of *i*-MAX single crystals.

The purpose of the present work is to report on the growth of $(Mo_{2/3}RE_{1/3})_2AlC$ (RE = Nd, Gd, Dy, Ho, Er) single crystals and to present their structural and dynamical (Raman spectra) properties, using both experimental and *ab initio* approaches. An analysis of the mode symmetries and of the relative atomic displacements allows for a deeper understanding of the changes in the Raman wave numbers with RE element. Similar studies were performed for a number of MAX phases, where Raman-active vibrational modes are measured and calculated *ab initio* [35–40]. In all cases, the low-wave-number modes, that ranged from 50 to 300 cm^{-1} were assigned to the vibrations of the M and A atoms; the X atoms vibrate at higher wave numbers, that range from 500 to 650 cm^{-1}, and

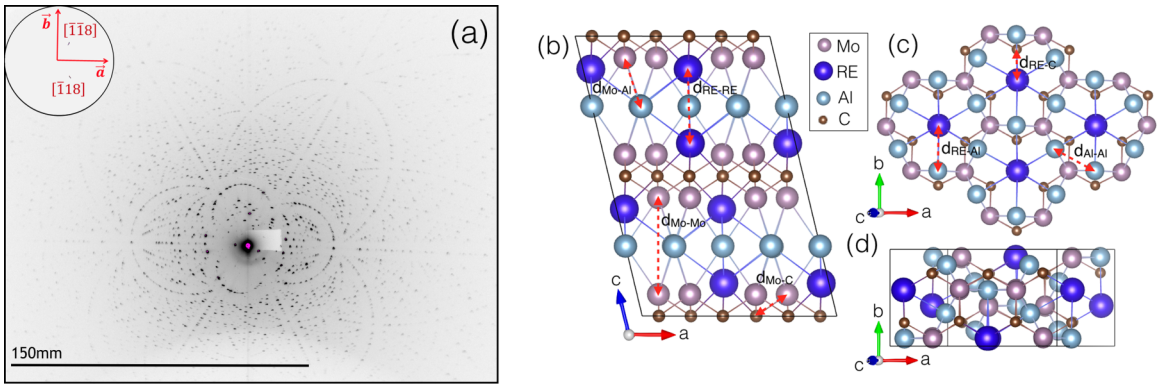

FIG. 1. (a) Laue diffraction pattern of $(Mo_{2/3}Ho_{1/3})_2AlC$ single crystal, obtained in transmission, along with a pole figure. Schematic representation of the conventional monoclinic $C2/c$ cell of $(Mo_{2/3}RE_{1/3})_2AlC$, RE = Nd, Gd, Dy, Ho, or Er, along the, (b) [010] and, (c) and (d) [103] zone axes. In (b) and (c), some characteristic interatomic distances, namely, $d_{Mo\text{-}Mo}$, $d_{Mo\text{-}Al}$, $d_{Mo\text{-}C}$, $d_{RE\text{-}RE}$, $d_{RE\text{-}Al}$, $d_{RE\text{-}C}$, and $d_{Al\text{-}Al}$, are defined with red dashed arrows; $d_{Mo\text{-}Mo}$ and $d_{RE\text{-}RE}$ are defined as the distances between two Mo/RE atoms separated by an Al plane. RE, Mo, Al, and C atoms are represented by dark blue, purple, light blue, and brown spheres, respectively.

were only observed in the 312 and 413 systems. In general, good agreement was observed between the first-principles calculations and the experimental measurements.

II. METHODS

A. Single-crystal growth

Single crystalline platelets of $(Mo_{2/3}RE_{1/3})_2AlC$ (RE = Nd, Gd, Dy, Ho, Er) were grown, using a high-temperature solution growth process similar to the one described in Refs. [29,30] for other MAX phase single crystals. First, Mo, RE, and Al are melted in a sealed graphite crucible at 1800 °C in an induction-heated reactor. A soaking time of a few hours is used to allow the Mo to melt and the C—from the crucible walls—to dissolve in the solution. After soaking, the temperature is reduced to 1500 °C in 0.5 h, and a linear cooling ramp of a few days, down to 800 °C, is used to nucleate and grow the crystals near the molten flux surface that is the coolest point. Since only the binary phase diagrams are known for the present systems, the solution compositions were chosen by systematically avoiding compositions lying close to any of the existing stable binary compounds. A favorable, and typical, Mo:RE:Al atomic composition is 0.1:0.45:0.45. Once cooled, the crystals are separated from the solidified flux by simply placing the latter for one to two days in ambient room temperature (RT). The excess RE oxidizes and transforms the flux into a purple (RE = Ho) or a grey (RE = Nd, Gd, Dy, and Er) powder, leaving behind flux-free, metallically shiny single crystals. Due to the structure anisotropy and the lack of screw dislocations, the silver-colored shiny platelets exhibit low aspect ratios. The largest platelet areas were around 3 mm^2 with thicknesses up to 100 μm.

B. X-ray diffraction

The metallic platelet $(Mo_{2/3}RE_{1/3})_2AlC$ single crystals were used to measure the x-ray intensity data, in transmission mode, for structural determination using a Bruker APEX2 SC diffractometer. The determination of the final cell constants is

TABLE I. Experimental and theoretical lattice parameters for the monoclinic $C2/c$ RE-containing i-MAX phases $(Mo_{2/3}RE_{1/3})_2AlC$ (RE = Nd, Gd, Dy, Ho, or Er).

Compounds	a (Å)	b (Å)	c (Å)	β (°)	V (Å^3)
$(Mo_{2/3}Nd_{1/3})_2AlC$					
Expt.	9.6598(4)	5.5896(2)	14.1599(5)	103.474(2)	743.51(5)
Calc.	9.6964	5.6078	14.3021	103.4974	756.19
$(Mo_{2/3}Gd_{1/3})_2AlC$					
Expt.	9.5747(3)	5.5386(2)	14.0872(5)	103.532(2)	726.31(4)
Calc.	9.5903	5.5488	14.1782	103.5811	733.39
$(Mo_{2/3}Dy_{1/3})_2AlC$					
Expt.	9.5204(5)	5.5122(3)	14.0423(10)	103.559(2)	716.38(7)
Calc.	9.5475	5.5255	14.1290	103.5960	724.48
$(Mo_{2/3}Ho_{1/3})_2AlC$					
Expt.	9.4905(6)	5.4956(3)	14.0163(8)	103.559(2)	710.66(7)
Calc.	9.5283	5.5151	14.1078	103.5992	720.57
$(Mo_{2/3}Er_{1/3})_2AlC$					
Expt. [26]	9.49271	5.49282	14.01770	103.5300	710.623
Calc.	9.5111	5.5076	14.0838	103.5968	717.09

TABLE II. Calculated structural parameters for the monoclinic $C2/c$ RE-containing i-MAX phases $(Mo_{2/3}RE_{1/3})_2AlC$ (RE = Nd, Gd, Dy, Ho, or Er).

Compound	Lattice parameters (Å, °)	Atom	Wyckoff site	Reduced coordinates		
$(Mo_{2/3}Nd_{1/3})_2AlC$	$a = 9.6964$	Nd1	$8f$	0.9615	0.4197	0.1213
	$b = 5.6078$	Mo1	$8f$	0.6092	0.4024	0.0746
	$c = 14.3021$	Mo2	$8f$	0.7310	0.5754	0.9253
	$\alpha = 90.0000$	Al1	$4e$	0.0000	0.9193	0.2500
	$\beta = 103.4974$	Al2	$8f$	0.7500	0.8370	0.7519
	$\gamma = 90.0000$	C1	$4d$	0.2500	0.2500	0.5000
		C2	$8f$	0.4103	0.2680	0.0000
$(Mo_{2/3}Gd_{1/3})_2AlC$	$a = 9.5903$	Gd1	$8f$	0.9608	0.4193	0.1185
	$b = 5.5488$	Mo1	$8f$	0.6097	0.4038	0.0760
	$c = 14.1782$	Mo2	$8f$	0.7297	0.5763	0.9240
	$\alpha = 90.0000$	Al1	$4e$	0.7489	0.8383	0.7517
	$\beta = 103.5811$	Al2	$8f$	0.0000	0.9198	0.2500
	$\gamma = 90.0000$	C1	$4d$	0.2500	0.2500	0.5000
		C2	$8f$	0.4123	0.2622	0.0000
$(Mo_{2/3}Dy_{1/3})_2AlC$	$a = 9.5485$	Dy1	$8f$	0.9605	0.4192	0.1173
	$b = 5.5255$	Mo1	$8f$	0.6099	0.4043	0.0766
	$c = 14.1290$	Mo2	$8f$	0.7292	0.5767	0.9234
	$\alpha = 90.0000$	Al1	$4e$	0.0000	0.9204	0.2500
	$\beta = 103.5960$	Al2	$8f$	0.7483	0.8380	0.7517
	$\gamma = 90.0000$	C1	$4d$	0.2500	0.2500	0.5000
		C2	$8f$	0.4132	0.2599	0.0000
$(Mo_{2/3}Ho_{1/3})_2AlC$	$a = 9.5283$	Ho1	$8f$	0.9603	0.4192	0.1167
	$b = 5.5151$	Mo1	$8f$	0.6099	0.4046	0.0769
	$c = 14.1078$	Mo2	$8f$	0.7290	0.5769	0.9232
	$\alpha = 90.0000$	Al1	$4e$	0.0000	0.9207	0.2500
	$\beta = 103.5992$	Al2	$8f$	0.7480	0.8392	0.7516
	$\gamma = 90.0000$	C1	$4d$	0.2500	0.2500	0.5000
		C2	$8f$	0.4135	0.2588	0.0000
$(Mo_{2/3}Er_{1/3})_2AlC$	$a = 9.5111$	Ho1	$8f$	0.9602	0.4193	0.1161
	$b = 5.5076$	Mo1	$8f$	0.6100	0.4049	0.0771
	$c = 14.0838$	Mo2	$8f$	0.7289	0.5770	0.9231
	$\alpha = 90.0000$	Al1	$4e$	0.0000	0.9210	0.2500
	$\beta = 103.5968$	Al2	$8f$	0.7476	0.8395	0.7515
	$\gamma = 90.0000$	C1	$4d$	0.2500	0.2500	0.5000
		C2	$8f$	0.4139	0.2576	0.0000

based upon the refinement of the XYZ centroids of reflections above $20\sigma(I)$. Data were corrected for absorption effects using the Numerical Mu from formula method (SADABS). The structure was solved, and refined, using the Bruker SHELXTL software package [41]. Several different single crystals for each RE element were examined in order to ascertain that all gave the same structure.

C. Scanning transmission electron microscopy

Scanning transmission electron microscopy (STEM) combined with high angle annular dark field imaging (STEM-HAADF) was performed in a double-correlated FEI Titan^3, operated at 300 kV.

D. Raman spectroscopy

Single-crystal Raman spectra were recorded using a Horiba/Jobin Yvon LabRam spectrometer equipped with a liquid-nitrogen-cooled charge-coupled device detector. The measurements were carried out in the micro-Raman mode at RT in a backscattering geometry. The 514.5 nm, or 488 nm (Er-based phase), exciting line of an Ar^+ laser was focused to a spot size of $\sim 1\ \mu$m on the sample surface (i.e., basal plane) with an incident power of 1.8 and 1.1 mW for the Ho and Er-based phases, respectively, and 0.7 mW for the three other phases. The Raman spectra were calibrated using a silicon reference spectrum.

E. Computational details

The structural, electronic, and dynamical properties of the five $(Mo_{2/3}RE_{1/3})_2AlC$ compounds were computed *ab initio* using density functional theory (DFT) [42,43] and density functional perturbation theory (DFPT) [44–48], respectively, using the ABINIT package [49–51] which is based on plane-wave basis sets to represent the Kohn-Sham

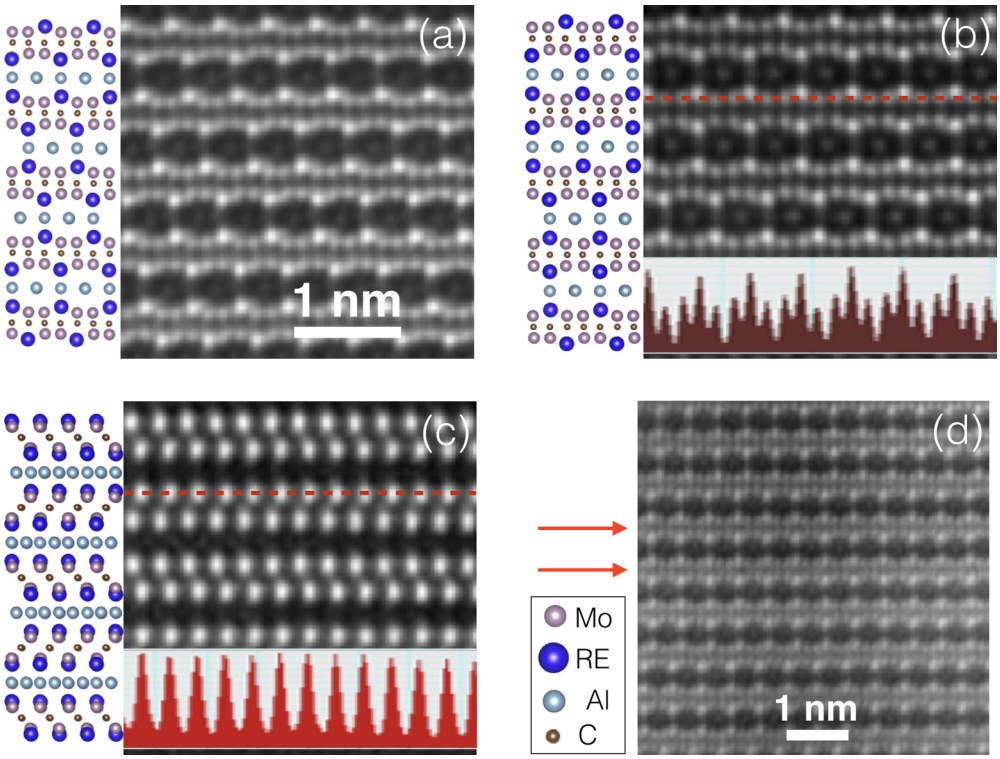

FIG. 2. High-resolution STEM images for $(Mo_{2/3}Dy_{1/3})_2AlC$ single crystals along (a) [010], (b) [110], and (c) [100] zone axes, with corresponding schematics for the $C2/c$ monoclinic structure. Insets in (b) and (c) show line profiles of the Z contrast along the red dashed lines. (d) Region with stacking faults shown by red arrows.

orbitals and charge density. The exchange-correlation functional was approximated using the generalized gradient approximation (GGA) as proposed by Perdew, Burke, and Ernzerhof (PBE) [52]. Following previous works on RE-containing MAX phases [25–27], the non-spin-polarized approach was considered. Optimized norm-conserving Vanderbilt pseudopotentials (ONCVPSP-PBE) [53] were used to describe core-valence interaction. Configurations of C-$2s^2 2p^2$, Al-$3s^2 3p^1$, Mo-$4s^2 4p^6 4d^5 5s^1$, Nd-$5s^2 5p^6 5d^1 6s^2$, Gd-$5s^2 5p^6 5d^1 6s^2$, Dy-$5s^2 5p^6 5d^1 6s^2$, Ho-$5s^2 5p^6 5d^1 6s^2$, and Er-$5s^2 5p^6 5d^1 6s^2$ were treated as valence electrons. A plane-wave kinetic energy cut-off of 40 Hartree was determined through a careful convergence investigation. The first Brillouin zone was sampled with a $12 \times 12 \times 12$ Monkhorst-Pack k-point grid, and a Gaussian smearing of 1 mHa was used to accelerate the convergence. Starting from the experimental x-ray diffraction (XRD) data, lattice parameters and atomic positions were fully optimized until the largest force was smaller than 2.5×10^{-4} eV/Å.

III. RESULTS AND DISCUSSION

A. RE-*i*-MAX crystal structures

A typical x-ray Laue diffraction pattern of a Ho-based single crystal is shown in Fig. 1(a), with a pole figure corresponding to a reflection orientation $[\bar{1}\bar{1}8]$. The conventional $(Mo_{2/3}RE_{1/3})_2AlC$ unit cell includes 48 atoms—16 Mo, 8 RE, i.e., Nd, Gd, Dy, Ho or Er, 12 Al, and 12 C atoms—and crystallizes in the $C2/c$ space group [Figs. 1(b)–1(d)] [26]. The nonequivalent atomic positions are distributed in specific Wyckoff positions: 8f (two Mo, one RE, one Al, and one C), 4e (one Al), and 4d (one C). The refined lattice parameters of the samples are listed in Table I and compared to the theoretically predicted parameters of the monoclinic structures. The complete set of cell parameters resulting from the structural optimization of the five considered compounds are reported in Table II. Note that, following experimental convention, the structural parameters in Tables I and II are for the conventional unit cell, corresponding to twice the primitive cell. Taking into account their similar structures, a schematic representation valid for any RE element is used in Figs. 1(b)–1(d).

Figures 2(a)–2(c) show STEM images of the $(Mo_{2/3}Dy_{1/3})_2AlC$ single-crystal sample along [010], [110], and [100] zone axes, respectively. In these micrographs, the Dy atoms appear as bright dots due to their large atomic number (Z contrast), the Mo atoms are less bright, the Al are almost invisible, and lastly, the C atoms are not visible. Line profiles in the insets of Figs. 2(b) and 2(c) show the Z contrast variation. In Fig. 2(b), the alternation of one strong peak and two weak peaks corresponds to the alternation of one RE atom and two Mo atoms. Schematics are shown to the left of each image. The structure is consistent with $C2/c$ space group. Most of the studied regions are free of faults as shown in Figs. 2(a)–2(c). The main defects observed in this family of materials are stacking faults. Figure 2(d) shows a region with stacking faults. As discussed in Ref. [26], in the $C2/c$ structure, every metal carbide layer is rotated by 60° with respect to others. In the *Cmcm* structures, on the other hand, layers are rotated by 180° with respect to each

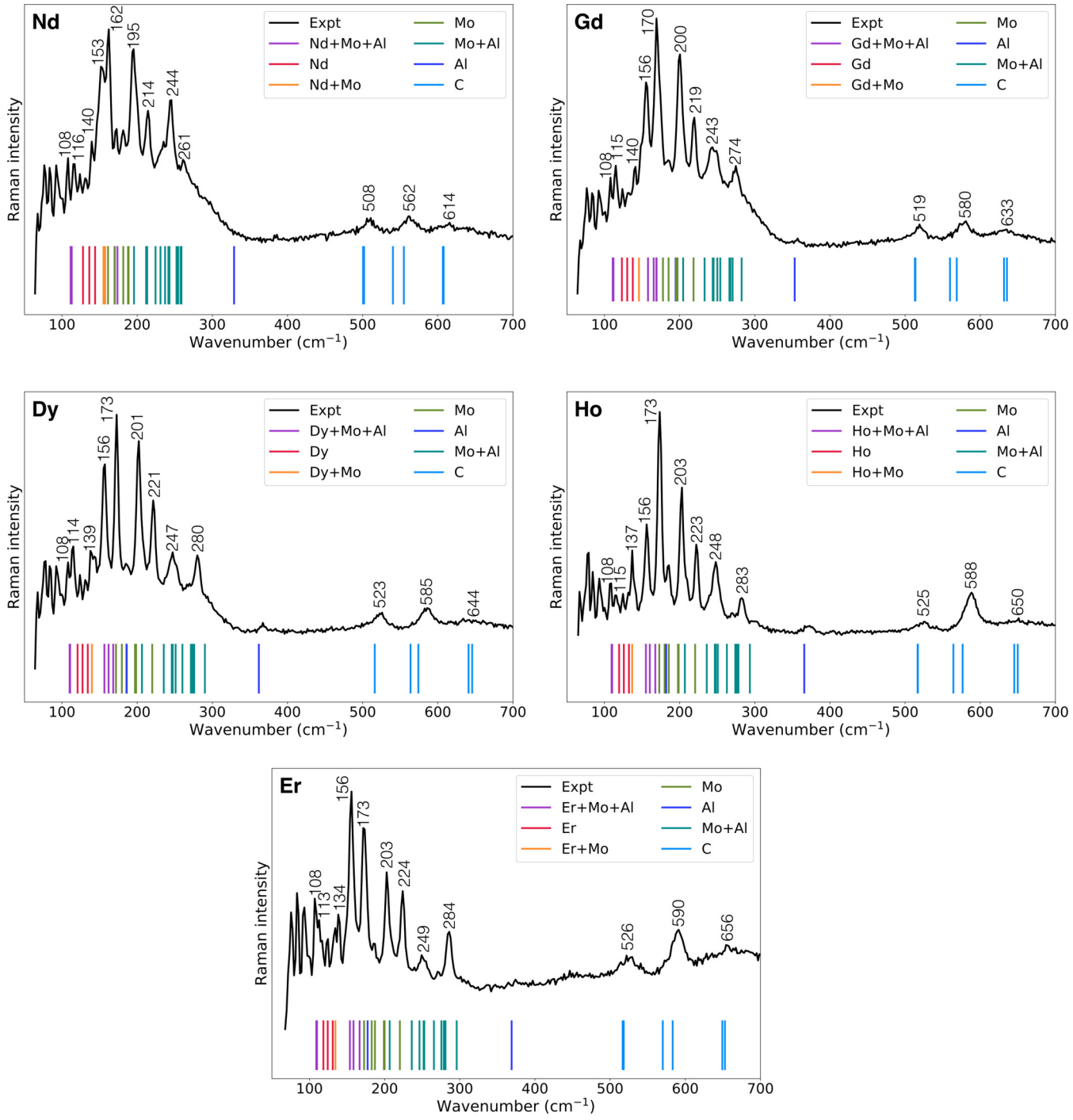

FIG. 3. Typical single-crystal $(Mo_{2/3}RE_{1/3})_2AlC$ (RE = Nd, Gd, Dy, Ho, Er) Raman spectra collected at room temperature. The 33 calculated Raman-active modes are represented at the bottom of each graph, and classified according to the atoms involved in the vibrational modes (see colored lines in inset).

other. In the stacking fault region, several layers are rotated by 180°, which reflects the structural similarity between the two structures.

B. Vibrational properties

With 24 atoms in the primitive cell, group theory predicts three acoustic modes and 69 optical modes at the Γ point of the Brillouin zone. Group theory can also determine which of these modes are Raman-active. The optical phonon modes can be classified with the following irreducible representation:

$$\Gamma_{\text{optical}} = \underbrace{16A_g + 17B_g}_{\text{Raman}} + \underbrace{18A_u + 18B_u}_{\text{IR}}, \quad (1)$$

where IR refers to infrared-active modes.

Typical Raman spectra of the crystals studied herein are shown in Fig. 3 and a summary of the results are listed in

TABLE III. Experimentally observed (ω_{exp}) and calculated (ω_{calc}) Raman mode wave numbers in $(Mo_{2/3}RE_{1/3})_2AlC$, with RE = Nd, Gd, Dy, Ho, Er. The symmetry of each mode is noted as well as the atoms involved in the vibrations. Atoms in between brackets refer to the Nd-based system, and atoms in between squared brackets refer to the four other systems. Wave numbers of intense peaks are highlighted in bold. These peaks form the Raman fingerprint of RE-*i*-MAX phases.

		Nd		Gd		Dy		Ho		Er	
Symmetry	Atoms	ω_{exp}	ω_{calc}	ω_{exp}	ω_{calc}	ω_{exp}	ω_{calc}	ω_{exp}	ω_{calc}	ω_{exp}	ω_{calc}
$A_g(1)$	RE+Mo+Al	**108**	111.5	**108**	111.2	**108**	110.1	**108**	109.5	**108**	109.1
$B_g(1)$	RE+Mo+Al	**116**	112.9	**115**	112.0	**114**	110.8	**115**	110.2	**113**	110.0
$B_g(2)$	RE	124	127.9	124	123.2	124	120.7	124	119.5	124	118.5
$A_g(2)$	RE	131	136.3	132	130.3	131	127.3	132	125.8	130	124.3
$B_g(3)$	RE	**140**	144.0	**140**	137.7	**139**	134.3	**137**	132.6	**134**	131.0
$A_g(3)$	RE+Mo	147	155.2	148	145.9	144	139.8	140	136.8	139	134.5
$A_g(4)$	RE+Mo[+Al]	**153**	157.2	**156**	157.9	**156**	156.4	**156**	155.1	**156**	153.8
$B_g(4)$	RE+Mo+Al	160	170.0	–	165.5	151	162.0	152	160.3	152	158.6
$A_g(5)$	RE+Mo+Al	172	173.7	165	169.4	–	168.1	169	167.6	–	166.7
$B_g(5)$	Mo	**162**	161.2	**170**	169.0	**173**	171.8	**173**	172.9	**173**	172.7
$A_g(6)$	Mo	–	170.1	173	177.8	–	179.6	178	180.0	186	181.8
$B_g(6)$	Mo	181	181.5	182	185.3	185	185.6	190	185.9	191	187.1
$A_g(7)$	Al(+Mo)	211	213.3	187	194.7	188	186.1	185	182.1	–	177.4
$B_g(7)$	Mo	**195**	187.8	**200**	195.2	**201**	197.1	**203**	197.8	**203**	199.0
$A_g(8)$	Mo	192	188.6	–	197.2	–	198.6	205	198.7	–	200.0
$B_g(8)$	Mo+Al	200	195.8	205	204.7	208	206.4	210	207.0	209	206.7
$A_g(9)$	Mo(+Al)	**214**	211.9	**219**	218.5	**221**	220.0	**223**	220.6	**224**	220.8
$B_g(9)$	Mo+Al	228	224.4	232	233.2	237	235.4	239	236.1	240	236.1
$A_g(10)$	Mo+Al	235	231.0	240	244.0	243	246.0	244	246.8	245	246.4
$B_g(10)$	Mo+Al	**244**	241.5	**243**	245.2	**247**	247.3	**248**	248.3	**249**	251.9
$A_g(11)$	Mo+Al	241	243.0	249	250.2	252	251.2	253	250.9	255	252.8
$B_g(11)$	Mo+Al	238	237.1	255	254.1	259	260.2	262	262.9	259	265.6
$B_g(12)$	Mo+Al	256	254.6	271	266.2	266	271.5	270	274.0	272	275.5
$A_g(12)$	Mo+Al	249	252.3	278	267.7	270	273.8	275	276.3	280	278.7
$A_g(13)$	Mo+Al	**261**	257.8	**274**	270.5	**280**	275.9	**283**	278.3	**284**	281.0
$B_g(13)$	Mo+Al	263	258.9	285	282.5	293	290.1	296	293.5	297	295.9
$B_g(14)$	Al	–	328.9	357	353.1	367	361.9	372	365.8	376	369.0
$B_g(15)$	C	500	500.5	509	513.0	514	516.1	516	516.6	517	516.7
$A_g(14)$	C	**508**	501.9	**519**	513.7	**523**	516.1	**525**	517.0	**526**	518.1
$A_g(15)$	C	549	540.3	559	559.7	566	563.7	571	564.2	574	570.1
$B_g(16)$	C	**562**	554.8	**580**	568.7	**585**	574.1	**588**	576.5	**590**	583.3
$B_g(17)$	C	603	606.7	–	631.6	–	640.9	638	645.2	644	649.3
$A_g(16)$	C	**614**	607.8	**633**	635.5	**644**	645.7	**650**	649.9	**656**	652.8

Table III. Not surprisingly, the spectra are similar in shape and relative line intensities. As shown in Table III, the 33 expected Raman modes are observed for the Ho-based phase, while 31, 30, 29, and 30 modes are observed for the Nd, Gd, Dy, and Er-based phases, respectively. In all spectra, a majority of lines are located below 300 cm^{-1} and are distributed above a broad band. They are close to each other and most of them are well-defined, intense lines, whereas the seven last lines appear more dispersed over the 350–650 cm^{-1} range with rather weaker intensities.

The positions of the 33 Raman modes obtained theoretically by the *ab initio* calculations are also reported in Table III and represented using vertical lines under each experimental spectrum in Fig. 3. These vertical lines correspond to the atoms involved in the vibrational modes and are color coded (key is shown in insets). The comparison between experimental and calculated values in Table III indicates a quite good agreement for all the systems reported, with a maximal deviation of 7% for the low-wavenumber range [mode $B_g(4)$] and 2% for the high-wavenumber range [mode $B_g(16)$]. Such discrepancies can be linked to differences between experimental and theoretical atomic structures. Assignment of the computed Raman-active modes with the experimental peaks is almost straightforward even though no information regarding the peak intensities has been predicted theoretically.

By analyzing the symmetry of the vibrational modes (A_g and B_g modes listed in Table III) together with the atomic vibrations (eigendisplacements), a correspondence between the Raman-active modes of the five systems under study can be done. While the Gd-, Dy-, Ho-, Er-based phases possess very similar Raman behaviors including peaks positions, intensities, symmetries and atomic displacements, the Raman spectrum of the Nd-based phase is slightly different. Twelve relatively high-intensity peaks, present in the Raman spectra of all five systems, are identified as the fingerprint of the RE-*i*-MAX phases. These peaks are pointed out in the experimental spectra (Fig. 3) and are highlighted in bold in Table III. Moreover, they are schematically depicted in Fig. 4. Some

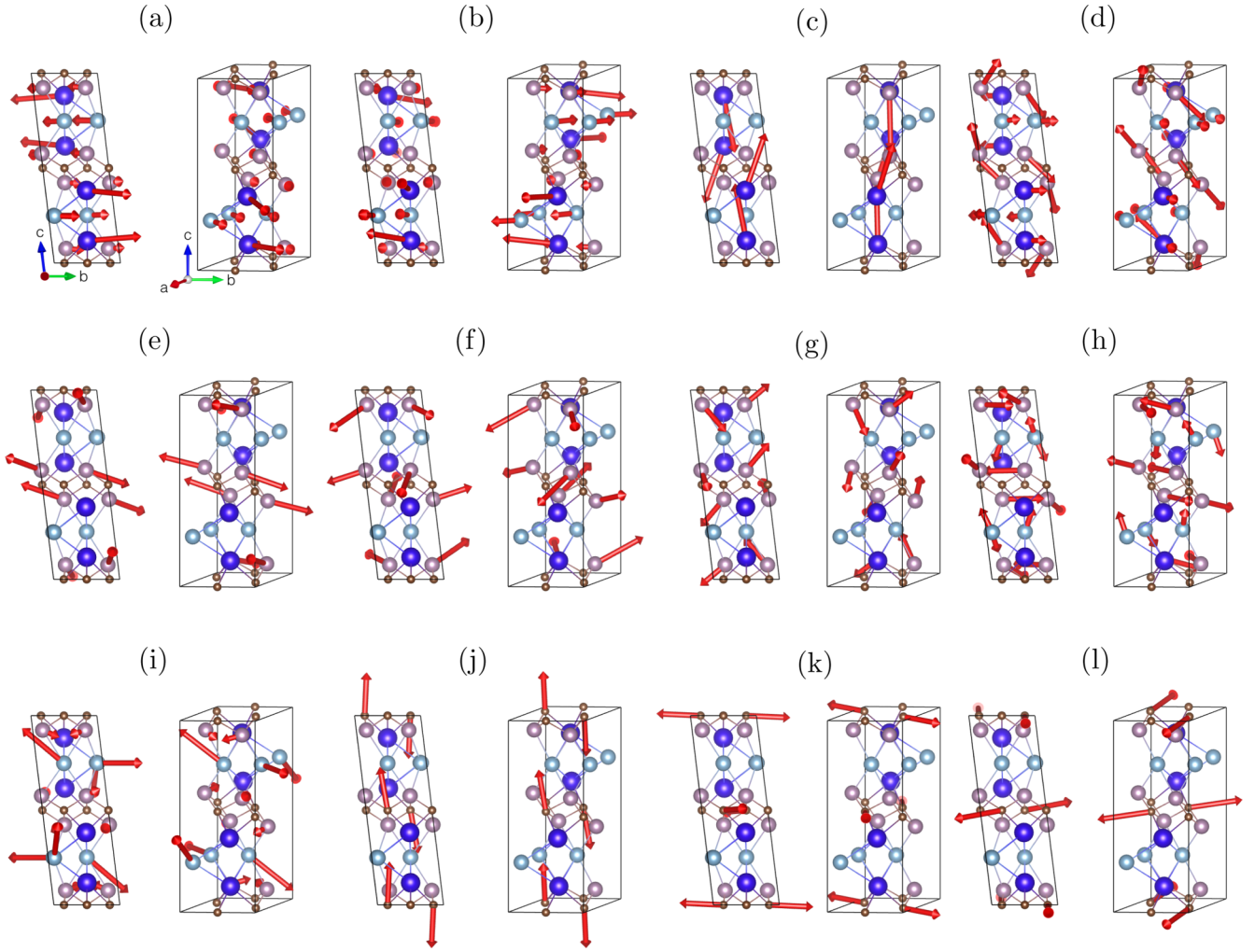

FIG. 4. Schematics of the atomic displacements (red arrows) of the representative vibrational modes of $(Mo_{2/3}RE_{1/3})_2AlC$ *i*-MAX phases: (a) $A_g(1)$ - RE+Mo+Al, (b) $B_g(1)$ - RE+Mo+Al, (c) $B_g(3)$ - RE, (d) $A_g(4)$ - RE+Mo+Al, (e) $B_g(5)$ - Mo, (f) $B_g(7)$ - Mo, (g) $A_g(9)$ - Mo, (h) $B_g(10)$ - Mo+Al, (i) $A_g(13)$ - Mo+Al, (j) $A_g(14)$ - C, (k) $B_g(16)$ - C, and (l) $A_g(16)$ - C. Atomic vibrations are similar for the five systems with RE = Nd, Gd, Dy, Ho, and Er, except for the modes $A_g(4)$, $A_g(7)$, and $A_g(9)$, as mentioned in Table III. The size of the arrows is proportional to the vibration amplitude and varies very slightly from one system to another. The vibrations in the Dy-based system are used for the schematics. Dy, Mo, Al, and C atoms are presented using dark blue, purple, light blue, and brown spheres, respectively.

weak additional lines are observed in the Raman spectra of all the compounds, although not predicted by theory. Typically, two to four additional lines are observed in the spectra depending on the RE element in the mid-wave-number range [between modes $B_g(13)$ and $B_g(14)$], and one (Dy-, Ho-based phases) or two (Nd-, Gd-, Er-based phases) additional lines in the higher wave-number part of the spectra. These lines remain presently unassigned and could possibly be due to other undefined phases present in the samples. In the same way, four low-wave-number peaks respectively located around 67, 77, 84, and 93 cm^{-1} were observed in the experimental spectra of the five systems and not predicted theoretically. Even though Raman measurements were performed under atmosphere, we are not sure at this stage whether this explains the presence of these low-wave-number Raman peaks. Mercier *et al.* [37] reported the Raman spectrum of Ti_3SiC_2 and assigned the nonpredicted low-wavenumber modes to the presence of air, including one peak at 83 cm^{-1} and another at 92 cm^{-1}. Even with this assumption, the first two peaks observed in the Raman spectra of the RE-*i*-MAX phases remain unassigned. These peaks may be due to other undefined phases present in the samples.

In order to understand the effects of mass and bond stiffness on the Raman peak positions, we used the conventional expression for vibrational wave numbers, assuming harmonic oscillation, given by [35]

$$\omega = \sqrt{\frac{K}{m_{\text{red}}}}, \tag{2}$$

where K is the bond stiffness and m_{red} is the reduced mass of the atomic masses of the species involved in the vibrations. Because the C atoms are light, and as typical of the MAX phases in general [35–40], they tend to form strong covalent bonds with Mo, and their vibrations are exclusively located in the high-wave-number ($\omega \geqslant 500$ cm^{-1}) range. Due to the lower symmetry of the *i*-MAX phases, this is the first time C atom vibrations are involved

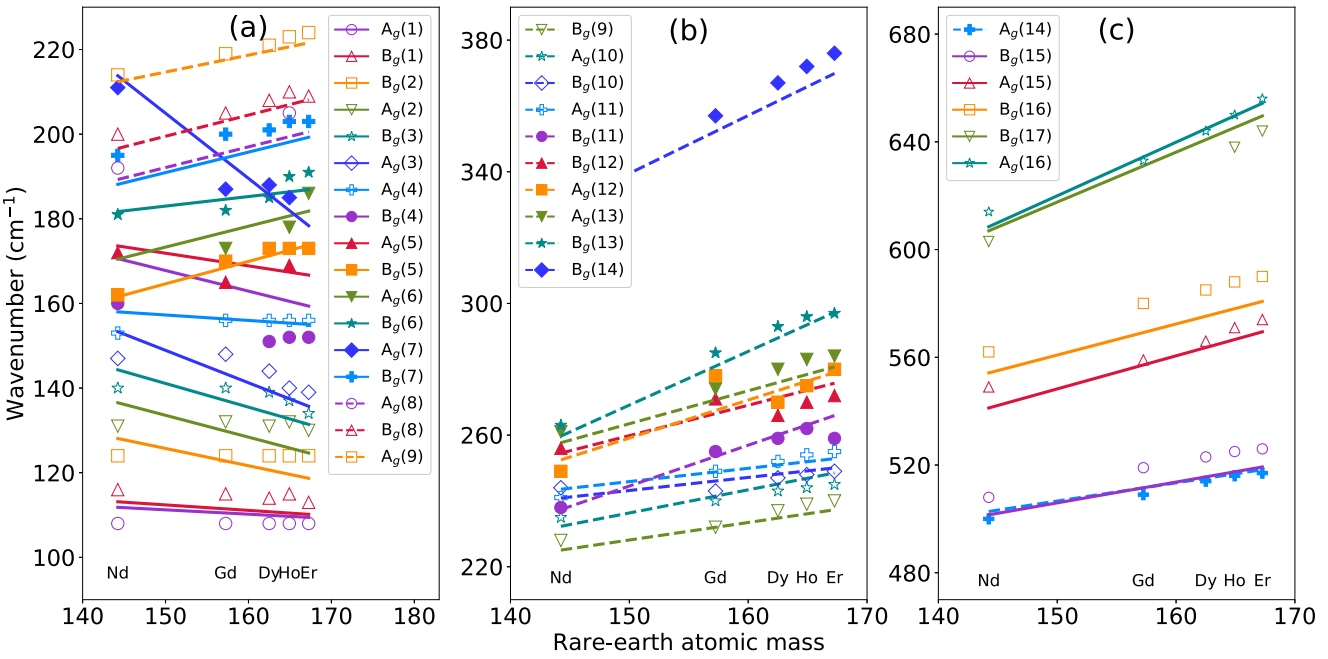

FIG. 5. Dependence of both experimental and calculated wave numbers on rare-earth atomic mass, for the 33 Raman-active modes. For each mode, the experimental data are represented by markers of the same color for the five RE-*i*-MAX phases. Moreover, a least squares polynomial fit of the theoretical values obtained by DFT (not shown here) is represented by a straight line with the same color as the markers related to the experimental data. These lines allow for a better understanding of the evolution of the wave numbers with the RE atomic mass. The slopes of the lines related to the first nine modes and $A_g(7)$ are negative, while the ones for the other 23 modes are positive.

in Raman-active modes in a 211 MAX phase [35,39]. The relative positions of the vibrational modes involving the RE, Mo, and Al atoms exhibit a less clear trend and vary from one phase to another. Nevertheless, the vibrational modes involving the RE atoms—because of their mass and the weaker bonds they form with Al and C—are mostly located in the low-wave-number ($\omega \leqslant 180$ cm^{-1}) range. A detailed analysis of bond strengths in $(M^1_{2/3}M^2_{1/3})_2AlC$ was also reported by Dahlqvist *et al.* [54] leading to the following classification: M^1-C > M^2-C > M^1-Al > M^2-Al, where M^1 and M^2 would respectively correspond to Mo and RE elements in our systems. The fact that the Sc atoms are readily etched from the $(Mo_{2/3}Sc_{1/3})_2AlC$ *i*-MAX phase to form the $Mo_{1.33}C$ MXene [24] supports this assumption.

To further explore the specific role of RE atomic mass, m_R, and bond stiffness, K, on the Raman peak positions, the evolution of the mode wave numbers as a function of m_{RE} is presented in Fig. 5. In this figure, the data points are those obtained experimentally and the lines are obtained from a least squares polynomial fit of the theoretical values. In Fig. 5(a), the first nine modes are associated with the vibrations of the RE atoms, the next eight—with the exception of $A_g(7)$ where Al predominates—relate to the vibrations of the Mo atoms. Similarly, the set of lines in the 220–300 cm^{-1} range in Fig. 5(b) relate to the Mo atoms, while the isolated one above 320 cm^{-1} is due to Al atom vibrations alone. Lastly, Fig. 5(c) plots the six highest energy modes that involve the C atoms. Some of these modes are schematically illustrated

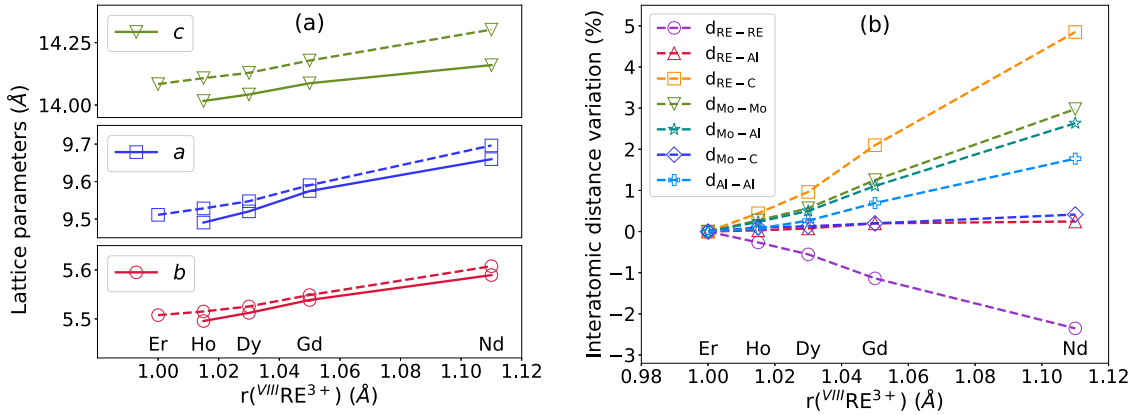

FIG. 6. Evolution of (a) lattice parameters *a*, *b*, and *c*, and (b) interatomic distances with the effective ionic radius of the RE element at valence +3 and coordination VIII. The variations of interatomic distances are normalized using those of the Er-based phase, and expressed in percents. Solid and dashed lines correspond to the parameters for the experimental and relaxed structures, respectively.

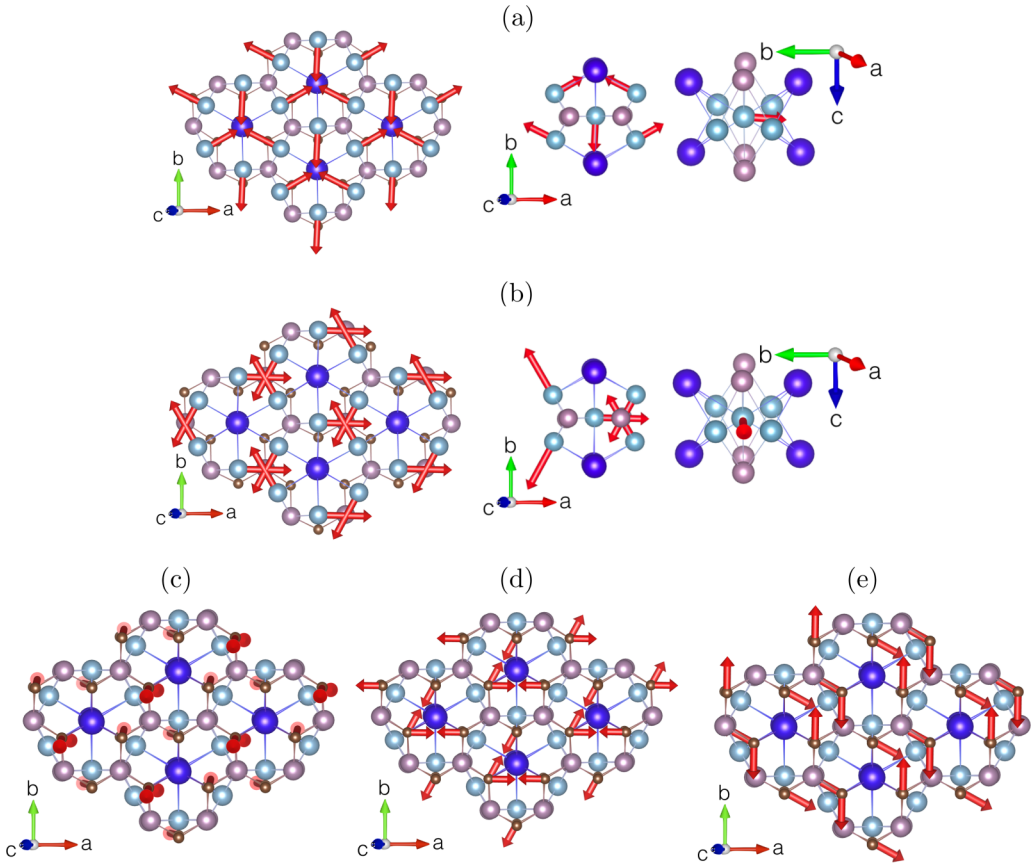

FIG. 7. Representation of the outlying Al modes: (a) $A_g(7)$ and (b) $B_g(14)$, and C-related modes: (c) $A_g(14)$, (d) $B_g(16)$, and (e) $A_g(16)$, aiming at better visualizing the direction of the vibrations with respect to the direction of the various bonds. The vibrations in the Dy-based system are used for the schematics. Dy, Mo, Al, and C atoms are presented using dark blue, purple, light blue, and brown spheres, respectively.

in Fig. 4. When analyzing the results in Fig. 5, the following observations are salient.

(a) With one notable exception, viz.$A_g(7)$ discussed below, above $\sim$160 cm^{-1} the experimental points and the slopes of the lines predicted by DFT, change from negative to positive [Fig. 5(a)].

(b) For some of the modes between 100 and 200 cm^{-1}, the experimental results are not as well captured by theory. For example, experimentally the first four modes are flat, while DFT predict a slightly negative slope. Others are flat and then drop off [e.g., $B_g(3)$, $A_g(3)$, etc. in Fig. 5(a)]. It appears that at the lowest wave numbers, the DFT calculations either overestimate or underestimate K.

(c) Above $\sim$220 cm^{-1} [Figs. 5(b) and 5(c)], the agreement between theory and experiment can be considered qualitatively satisfying in that the slopes of the lines faithfully reproduce those of experimental data points. With a few exceptions—e.g., $A_g(12)$ and $B_g(16)$—the quantitative agreement is also quite correct.

According to Eq. (2), if K is not a function of composition, then the mode energies should decrease with increasing m_{RE}. In contrast, if K increases faster than m_{RE}, then the slopes should be positive. Lastly, if the ratio K/m_{RE} remains constant, the energies should not vary with composition. How this concept in essence explains the trends observed in Fig. 5 is discussed below.

More specifically, according to Table III, the heavy RE elements participate in the first nine modes, where presumably mass is important. It is thus not a coincidence that the energies of these modes are either not a function of m_{RE} or they decrease with increasing m_{RE}. This agreement can thus be taken as an independent confirmation of, at least, the correctness of assigning the first nine modes with vibrations of the RE elements.

Before discussing the rest of the modes, refer to Fig. 6, where the experimental (solid lines) and optimized (dashed lines) lattice parameters, and various bond distances are plotted as a function of the effective ionic radii of the RE^{3+} cations. Given that shorter bonds are stronger, as verified through *ab initio* calculations for the systems under study, then, from Fig. 6(b), we conclude that (i) the RE-RE bonds are strongest for Nd and weakest for Er. It is thus not too surprising that the modes involving Nd atoms have higher wavenumbers with respect to the others [Fig. 5(a)]. (ii) The Mo-Mo, Al-Al, Mo-Al, and, especially, the RE-C bonds, are weakest for Nd and strongest for Er, which explains the increasing wave numbers (again with a notable exception) going from the left to right in Figs. 5(a)–5(c).

We now focus on the two outlying modes—$A_g(7)$ and $B_g(14)$—involving only the Al atoms. To understand their evolution it is important to consider the respective directions of the vibrations with respect to the bond directions. This

is important because for vibrations involving more than one bond, the contribution to the energy of the bond parallel to the vibrational direction is larger than the one perpendicular to it. As a consequence, for similar bond stiffnesses, the first type influences K more, and concomitantly ω, than the second one.

Mode $A_g(7)$ corresponds to the well-known torsional mode observed in 2D kagome lattices [55–57]. As depicted in Fig. 7(a), the Al atoms are vibrating in the *ab* plane with a vibrational direction parallel to the projection of the RE-Al bonds and perpendicular to the projection of the Mo-Al bonds in the *ab* plane. Therefore the bonding governing the stiffness is mostly that of the RE-Al one. Since the RE-Al distance is not a function of composition [Fig. 6(b)] then K should not be either. Therefore the only variable here is the vibrational direction. Based on previous results by Dahlqvist *et al.* [54], a difference in atomic radii between the Mo and RE atoms induces a displacement of RE atoms towards the Al plane, in order to minimize the in-plane stress. The larger the RE ionic radius, the larger the out-of-plane shift. Hence, the out-of-plane RE-RE distance decreases when increasing RE ionic radii [Fig. 6(b)]. Furthermore, as the unit cell expands when the atomic radius of the RE element increases [Fig. 6(a)], the in-plane spacing between Al atoms increases. As a consequence, RE-Al bonding lengths are comparable for the five systems, but the angle between the Al plane and the RE-Al bonds decreases with increasing ionic radii. This probably explains the decreasing wave numbers observed for mode $A_g(7)$ going from left to right in Fig. 5(a).

Mode $B_g(14)$ also involves in-plane vibrations of Al atoms [Fig. 7(b)]. In contrast with mode $A_g(7)$, here the motion of the Al atoms is parallel to the projection of the Mo-Al bonds in the *ab* plane and perpendicular to the one of the RE-Al bonds. Therefore the Mo-Al bond stiffness should prevail in the K factor. The positive slope in Fig. 5(b) of this mode thus indirectly confirms the increasing value of Mo-Al bond stiffnesses with the RE atomic mass.

Eventually, the dispersion from 500 to 650 cm^{-1} observed in Fig. 5(c) for the six C-related modes can be assigned to the various directionalities of the C vibrations with respect to atomic bonds. Modes $B_g(15)$ and $A_g(14)$ correspond to out-of-plane vibrations of C atoms [Fig. 4(j)], perpendicular to both Mo-C and RE-C bonds [Fig. 7(c)]. Therefore the stiffness factor only slightly reflects the stiffness of Mo-C and RE-C bonds. Modes $A_g(15)$ and $B_g(16)$ correspond to in-plane vibrations of C atoms [Fig. 4(k)], with a vibrational direction almost parallel to the projection of the RE-C bonds and perpendicular to the projection of the Mo-C bonds in the *ab* plane [Fig. 7(d)]. Therefore the bonding governing the stiffness is that of the RE-C one. In contrast, in modes $B_g(17)$ and $A_g(16)$, C atoms are vibrating in a direction parallel to Mo-C bonds and perpendicular to RE-C bonds [Fig. 7(e)]. Therefore the bonding governing the stiffness is that of the Mo-C one. Since Mo-C bonds are stronger than RE-C bonds [54], it is not surprising to find the modes governed by the Mo-C bond stiffnesses at higher wave numbers than those governed by the RE-C one.

IV. CONCLUSIONS

In summary, we report on the growth and characterization of five representative members of the new family of rare-earth containing *i*-MAX single crystals, viz. $(Mo_{2/3}Nd_{1/3})_2AlC$, $(Mo_{2/3}Gd_{1/3})_2AlC$, $(Mo_{2/3}Dy_{1/3})_2AlC$, $(Mo_{2/3}Ho_{1/3})_2AlC$, and $(Mo_{2/3}Er_{1/3})_2AlC$. The structure determined by XRD is confirmed by STEM images as well as by a satisfying agreement between experimental and computed Raman wave numbers. As far as we are aware, this is the first report on the Raman spectra of the RE-*i*-MAX phases in general and single crystals in particular. The *ab initio* calculations of the vibrational properties include the determination of phonon mode wave numbers, symmetries and relative atomic displacements. A full analysis of the results is provided, as well as a comparison of the Raman spectra of the five systems. In this framework, the changes in mode wave numbers are explained by changes in RE mass and bond stiffnesses. From this analysis, twelve high-intensity Raman peaks, present in the five experimental spectra, are identified as the Raman fingerprint of the RE-*i*-MAX phases, thus allowing for the identification of *i*-MAX phases and the possible detection of defects, in future work.

ACKNOWLEDGMENTS

A.C. and J.-C.C. acknowledge financial support from the Fédération Wallonie-Bruxelles through the Action de Recherche Concertée (ARC) on 3D nanoarchitecturing of 2D crystals (No. 16/21-077), from the European Union's Horizon 2020 researchers and innovation program (No. 696656), and from the Belgium FNRS. LMGP was financially supported by the "Agence Nationale de la Recherche" (project ANR-18-CE09-0041). L.J. thanks UCA-PARTNER for the use of the Bruker SC-diffractometer. A.C., J.-C.C, and T.O. are also indebted to the Flag-ERA JTC 2017 project entitled "MORE-MXenes." M.W.B. acknowledges the financial support of the chair of excellence program of the Nanosciences Foundation (Université Grenoble-Alpes Foundation). J. R. and M. B. acknowledge support from the Swedish Foundation for Strategic Research (SSF) for Project Funding (EM16-0004), and from the Knut and Alice Wallenberg (KAW) Foundation for a fellowship grant, project funding (KAW 2015.0043), and for support to the Linköping electron microscopy laboratory. Computational resources were provided by the supercomputing facilities of the UCLouvain (CISM) and the Consortium des Equipements de Calcul Intensif en Fédération Wallonie-Bruxelles (CECI) funded by the Fonds de la Recherche Scientifique de Belgique (F.R.S.- FNRS) under convention No. 2.5020.11.

[1] M. W. Barsoum, Prog. Solid State Chem. **28**, 201 (2000).
[2] M. W. Barsoum, *MAX Phases*, 1st ed. (Wiley-Blackwell, 2013).
[3] M. W. Barsoum and T. El-Raghy, Am. Sci. **89**, 334 (2001).
[4] M. Nelson, M. T. Agne, B. Anasori, J. Yang, and M. W. Barsoum, Mater. Sci. Eng., A **705**, 182 (2017).
[5] M. Barsoum and G. Tucker, Scr. Mater. **139**, 166 (2017).
[6] M. W. Barsoum, X. Zhao, S. Shanazarov, A. Romanchuk, S. Koumlis, S. J. Pagano, L. Lamberson, and G. J. Tucker, Phys. Rev. Mater. **3**, 013602 (2019).

[7] M. Naguib, M. Kurtoglu, V. Presser, J. Lu, J. Niu, M. Heon, L. Hultman, Y. Gogotsi, and M. W. Barsoum, Adv. Mater. **23**, 4248 (2011).

[8] M. Naguib, O. Mashtalir, J. Carle, V. Presser, J. Lu, L. Hultman, Y. Gogotsi, and M. W. Barsoum, Acs Nano **6**, 1322 (2012).

[9] M. Naguib, V. N. Mochalin, M. W. Barsoum, and Y. Gogotsi, Adv. Mater. **26**, 992 (2014).

[10] B. Anasori, Y. Xie, M. Beidaghi, J. Lu, B. C. Hosler, L. Hultman, P. R. Kent, Y. Gogotsi, and M. W. Barsoum, ACS Nano **9**, 9507 (2015).

[11] M. R. Lukatskaya, B. Dunn, and Y. Gogotsi, Nat. Commun. **7**, 1 (2016).

[12] Q. Hu, D. Sun, Q. Wu, H. Wang, L. Wang, B. Liu, A. Zhou, and J. He, J. Phys. Chem. A **117**, 14253 (2013).

[13] M. Naguib, J. Halim, J. Lu, K. M. Cook, L. Hultman, Y. Gogotsi, and M. W. Barsoum, J. Am. Chem. Soc. **135**, 15966 (2013).

[14] M. Ghidiu, M. R. Lukatskaya, M. Q. Zhao, Y. Gogotsi, and M. W. Barsoum, Nature (London) **516**, 78 (2014).

[15] M. R. Lukatskaya, O. Mashtalir, C. E. Ren, Y. Dall'Agnese, P. Rozier, P. L. Taberna, M. Naguib, P. Simon, M. W. Barsoum, and Y. Gogotsi, Science **341**, 1502 (2013).

[16] Y. Dall'Agnese, M. R. Lukatskaya, K. M. Cook, P. L. Taberna, Y. Gogotsi, and P. Simon, Electrochem. Comm. **48**, 118 (2014).

[17] Y. Dall'Agnese, P. L. Taberna, Y. Gogotsi, and P. Simon, J. Phys. Chem. Lett. **6**, 2305 (2015).

[18] J. Come, J. M. Black, M. R. Lukatskaya, M. Naguib, M. Beidaghi, A. J. Rondinone, S. V. Kalinin, D. J. Wesolowski, Y. Gogotsi, and N. Balke, Nano Energy **17**, 27 (2015).

[19] S. Zhao, W. Kang, and J. Xue, Appl. Phys. Lett. **104**, 133106 (2014).

[20] T. Cabioch, P. Eklund, V. Mauchamp, M. Jaouen, and M. W. Barsoum, J. Eur. Ceram. Soc. **33**, 897 (2013).

[21] F. Meng, Y. Zhou, and J. Wang, Scr. Mater. **53**, 1369 (2005).

[22] A. Mockute, J. Lu, E. J. Moon, M. Yan, B. Anasori, S. J. May, M. W. Barsoum, and J. Rosen, Mater. Res. Lett. **3**, 16 (2015).

[23] Z. Liu, E. Wu, J. Wang, Y. Qian, H. Xiang, X. Li, Q. Jin, G. Sun, X. Chen, J. Wang, and M. Li, Acta Mater. **73**, 186 (2014).

[24] Q. Tao, M. Dahlqvist, J. Lu, S. Kota, R. Meshkian, J. Halim, J. Palisaitis, L. Hultman, M. W. Barsoum, P. O. Persson, and J. Rosen, Nat. Commun. **8**, 1 (2017).

[25] M. Dahlqvist, J. Lu, R. Meshkian, Q. Tao, L. Hultman, and J. Rosen, Sci. Adv. **3** (2017).

[26] Q. Tao, J. Lu, M. Dahlqvist, A. Mockute, S. Calder, A. Petruhins, R. Meshkian, O. Rivin, D. Potashnikov, E. Caspi, H. Shaked, A. Hoser, C. Opagiste, R.-M. Galera, R. Salikhov, U. Wiedwald, C. Ritter, A. R. Wildes, B. Johansson, L. Hultman, M. Farle, M. W. Barsoum, and J. Rosen, Chem. Mater. **31**, 2476 (2019).

[27] Q. Tao, T. Ouisse, D. Pinek, O. Chaix-Pluchery, F. Wilhelm, A. Rogalev, C. Opagiste, L. Jouffret, A. Champagne, J.-C. Charlier, J. Lu, L. Hultman, M. W. Barsoum, and J. Rosen, Phys. Rev. Mater. **2**, 114401 (2018).

[28] F. Mercier, T. Ouisse, and D. Chaussende, Phys. Rev. B **83**, 075411 (2011).

[29] T. Ouisse, E. Sarigiannidou, O. Chaix-Pluchery, H. Roussel, B. Doisneau, and D. Chaussende, J. Cryst. Growth **384**, 88 (2013).

[30] L. Shi, T. Ouisse, E. Sarigiannidou, O. Chaix-Pluchery, H. Roussel, D. Chaussende, and B. Hackens, Acta Mater. **83**, 304 (2015).

[31] T. Ouisse and M. W. Barsoum, Mater. Res. Lett. **5**, 365 (2017).

[32] T. Ouisse, L. Shi, B. A. Piot, B. Hackens, V. Mauchamp, and D. Chaussende, Phys. Rev. B **92**, 045133 (2015).

[33] T. Ito, D. Pinek, T. Fujita, M. Nakatake, S.-i. Ideta, K. Tanaka, and T. Ouisse, Phys. Rev. B **96**, 195168 (2017).

[34] A. Champagne, F. Bourdarot, P. Bourges, P. Piekarz, D. Pinek, I. Gélard, J.-C. Charlier, and T. Ouisse, Mater. Res. Lett. **6**, 378 (2018).

[35] N. J. Lane, M. Naguib, V. Presser, G. Hug, L. Hultman, and M. W. Barsoum, J. Raman Spectrosc. **43**, 954 (2012).

[36] O. D. Leaffer, S. Gupta, M. W. Barsoum, and J. E. Spanier, J. Mater. Res. **22**, 2651 (2007).

[37] F. Mercier, O. Chaix-Pluchery, T. Ouisse, and D. Chaussende, Appl. Phys. Lett. **98**, 081912 (2011).

[38] V. Presser, M. Naguib, L. Chaput, A. Togo, G. Hug, and M. W. Barsoum, J. Raman Spectrosc. **43**, 168 (2012).

[39] J. E. Spanier, S. Gupta, M. Amer, and M. W. Barsoum, Phys. Rev. B **71**, 012103 (2005).

[40] J. Wang, Y. Zhou, Z. Lin, F. Meng, and F. Li, Appl. Phys. Lett. **86**, 101902 (2005).

[41] G. M. Sheldrick, Acta Crystallogr. Sect. C **71**, 3 (2015).

[42] P. Hohenberg and W. Kohn, Phys. Rev. **136**, B864 (1964).

[43] W. Kohn and L. J. Sham, Phys. Rev. **140**, A1133 (1965).

[44] X. Gonze, Phys. Rev. B **55**, 10337 (1997).

[45] X. Gonze and C. Lee, Phys. Rev. B **55**, 10355 (1997).

[46] S. Baroni, P. Giannozzi, and A. Testa, Phys. Rev. Lett. **58**, 1861 (1987).

[47] X. Gonze, Phys. Rev. A **52**, 1086 (1995).

[48] S. Baroni, S. de Gironcoli, A. Dal Corso, and P. Giannozzi, Rev. Mod. Phys. **73**, 515 (2001).

[49] X. Gonze, J.-M. Beuken, R. Caracas, F. Detraux, M. Fuchs, G.-M. Rignanese, L. Sindic, M. Verstraete, G. Zerah, F. Jollet, M. Torrent, A. Roy, M. Mikami, P. Ghosez, J.-Y. Raty, and D. Allan, Comput. Mater. Sci. **25**, 478 (2002).

[50] X. Gonze, G. Rignanese, M. Verstraete, J. Betiken, Y. Pouillon, R. Caracas, F. Jollet, M. Torrent, G. Zerah, M. Mikami, P. Ghosez, M. Veithen, J.-Y. Raty, V. Olevano, F. Bruneval, L. Reining, R. Godby, G. Onida, D. Hamann, and D. Allan, Z. Kristallogr. **220**, 558 (2005).

[51] X. Gonze, B. Amadon, P.-M. Anglade, J.-M. Beuken, F. Bottin, P. Boulanger, F. Bruneval, D. Caliste, R. Caracas, M. Côté, T. Deutsch, L. Genovese, P. Ghosez, M. Giantomassi, S. Goedecker, D. Hamann, P. Hermet, F. Jollet, G. Jomard, S. Leroux, M. Mancini, S. Mazevet, M. Oliveira, G. Onida, Y. Pouillon, T. Rangel, G.-M. Rignanese, D. Sangalli, R. Shaltaf, M. Torrent, M. Verstraete, G. Zerah, and J. Zwanziger, Comput. Phys. Commun. **180**, 2582 (2009).

[52] J. P. Perdew, K. Burke, and M. Ernzerhof, Phys. Rev. Lett. **77**, 3865 (1996).

[53] D. R. Hamann, Phys. Rev. B **88**, 085117 (2013).

[54] M. Dahlqvist, A. Petruhins, J. Lu, L. Hultman, and J. Rosen, ACS Nano **12**, 7761 (2018).

[55] B. York, S. Solin, N. Wada, R. H. Raythatha, I. D. Johnson, and T. J. Pinnavaia, Solid State Commun. **54**, 475 (1985).

[56] T. C. Lubensky, C. L. Kane, X. Mao, A. Souslov, and K. Sun, Rep. Prog. Phys. **78**, 073901 (2015).

[57] T. Björkman, V. Skakalova, S. Kurasch, U. Kaiser, J. C. Meyer, J. H. Smet, and A. V. Krasheninnikov, ACS Nano **10**, 10929 (2016).